

# Optimization of Performance of Axial Turbines through Endwall Contouring

Duarte Filipe Cartaxo dos Santos  
duartefilipesantos@ist.utl.pt

Instituto Superior Técnico, Universidade de Lisboa, Portugal

December 2017

## Abstract

Nowadays, the performance improvement of turbomachinery through traditional methods have reached a plateau, so the state of the art optimization methods make use of computational fluid dynamics in order to solve fluid flow problems. The optimization methods using CFD are procedures with a high computational cost since a CFD simulation must be performed for each geometry generated by the optimization algorithm. Artificial neural networks can be used to approximate the CFD computations and reduce the computational power needed to perform an optimization. End wall profiling has been validated as an effective tool for the reduction of secondary losses in turbines. End wall profiling leads to fully three-dimensional hub and shroud surfaces. The aim of the end wall profiling is to reduce the transverse pressure gradient at the end wall through the principle of streamline curvature which results in reducing the blade loading in the end wall region and therefore controlling the end wall flows. This work consisted in performing three different optimization procedures (A, B and C). The results showed that the end wall profiling led to a considerable increase of the total-to-total efficiency. Optimization A led to an efficiency increase of 0.99%, optimization B increased 0.16% and optimization C increased 0.94%. This work shows that end wall contouring is a good technique to achieve improvement in the performance of a turbine. It also demonstrates that the use of optimization algorithms associated with the artificial neural networks is an innovative way of creating new improved geometries with less computational power.

**Keywords:** Turbomachinery, Computational Fluid Dynamics, Optimization Algorithm, Artificial Neural Networks, End Wall Contouring

## 1. Introduction

Turbomachinery describes machines that are responsible for the energy transfer between a rotor and a fluid flow. It includes both turbines and compressors which are rotary mechanical machines that work in a opposite way. While turbines transform the energy of the fluid into useful work, a compressor transfers energy from a rotor to a fluid.

One of the main reasons for the reduction of overall efficiency in turbomachinery is the secondary flows. The secondary flows can be categorized into different types of vortices, such as Horseshoe vortex, Passage vortex, Corner vortex and Tip Leakage vortex. These phenomena are represented in Figure 1.

A powerful method to improve the aerodynamic efficiency in a turbine by decreasing the occurrence of secondary flows is non-axisymmetric end wall profiling. The objective of the non-axisymmetric end wall profiling is to reduce the transverse passage pressure gradient by means of streamline curvature. This results in a reduction in the blade loading and

consequently controlling the flow.

Nowadays, the performance improvement of turbomachinery through traditional methods have reached a plateau so the state of the art optimization methods make use of the computational capacity available in the present days. Computational Fluid Dynamics (CFD) makes use of the most advanced numerical methods in order to solve and analyze fluid flow problems. CFD software are used both during the design phase and also for comparisons with the experimental results.

As technology develops and the computational power becomes greater, new and innovative softwares to optimize the geometry of turbomachinery components are created. Fine/Design3D is an integrated environment for the design and optimization of three-dimensional turbomachinery blades and channels. This environment integrates a modern parametric blade and non-axisymmetric end wall modeller, external CFD solver MULTI3 and a design and optimization environment for turbomachinery blades and channels. The design and

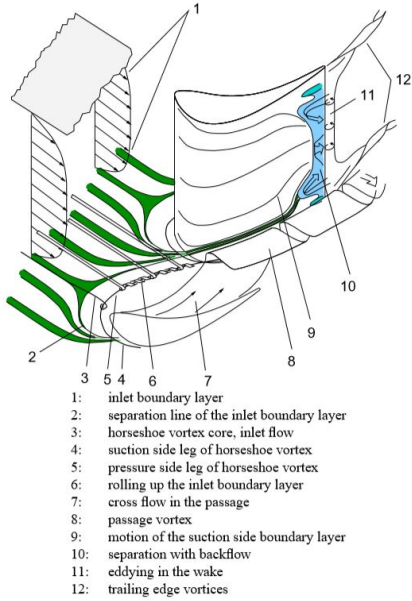


Figure 1: Secondary Flows Representation [1]

optimization environment makes use of optimization algorithms alongside the use of Artificial Neural Networks in order to approximate the CFD computation since it would be too costly to perform a CFD iteration for each different geometry generated by the optimization algorithm.

## 2. Secondary Flows in Turbomachines

As previously discussed, secondary flows are one of the main reasons for the overall efficiency decrease in turbomachinery. When secondary flows are mixing out, the secondary losses are generated.

In the year of 1955 Hawthorne [2] proposed his classical vortex model shown in Figure 2. In this model, Hawthorne states the existence of normal vorticity introduced by the inlet boundary layer. This normal vorticity at the inlet is responsible for the streamwise vorticity at the exit of a curved passage.

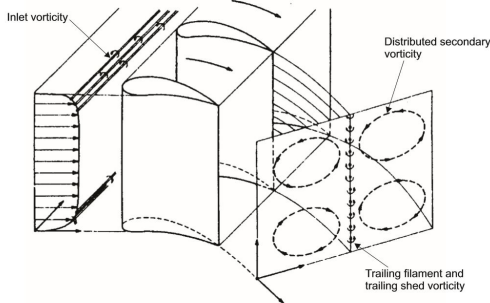


Figure 2: Secondary Flow Model by Hawthorne [2]

More recently, Langston [3] performed one of the first experimental investigations into the influence that end wall exerts in the flow. His experiments showed that the inlet boundary layer separates at the end wall of the cascade. As the working fluid progresses inside the cascade and encounters a solid turbomachinery component, such as a blade, the effects of longitudinal and vertical pressure gradients alongside the momentum deficit in the boundary layer, caused by the viscous effects, leads the flow to separate and form one or more vortices [4].

### 2.1. Methods to Control End Wall Flow

In order to attempt to control the end wall flow, several methods can be used. These methods can be divided into two categories, the active and passive methods. Active methods are of very limited success. An example of an active method for end wall flow control is boundary layer blowing investigated by Biesinger [5]. The passive methods for end wall flow control are the methods which researchers have dedicated more attention. The most frequently used are the blade leaning, axisymmetric and non-axisymmetric end wall profiling. Blade leaning has been investigated at the University of Cambridge by S.Harrison [6]. He reported that the blade leaning had no overall effect on loss, as it has more impact on establishing a more homogeneous flowfield going into the following airfoil rows. [6]

The concept of axisymmetric end wall contouring was introduced in the year of 1960 by the Russian engineers M.E. Dejc and A.E. Zarjankin. Since its conception several other engineers have studied this method for end wall flow control and it has been proven to be an efficient method for end wall flow.

In the year of 1965, Gilbert Rioulet [7] applied for a patent which would be the first generic geometry of a non-axisymmetric end wall titled "Curved Channels through which a gas or vapor flows". Non-axisymmetric end wall profiling leads to fully three-dimensional hub and shroud surfaces as opposed to the traditional design where the hub and shroud are surfaces of revolution. The aim of the end wall profiling is to reduce the transverse pressure gradient at the end wall through the principle of streamline curvature which results in reducing the blade loading in the end wall region and therefore controlling the end wall flows [8]. Concavity of the end wall results in a local increase of the static pressure as in a decrease of the flow velocity. On the other hand, convex curvature of the end wall will result in the opposite, the flow velocity will increase and the static pressure will drop locally, as we can see in Figure 3.

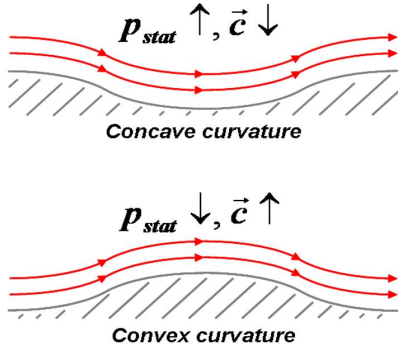


Figure 3: Convex and concave curvature influence in the end wall flow [9]

Not only can the concavity and convexity curvature mechanism be used but also different ones, such as the change of the cross sections which can affect the flow field over the span and not only locally as the previous mechanism. Another way to alter the flow would be the modification of the blockage through the thickening of the boundary layer. In conclusion, the objective of this alterations to the end wall geometry is to try to diminish the transverse pressure gradient as the driving force behind secondary flow by altering the static pressure on the suction and pressure surfaces [9].

### 3. Optimization Methodology

The method used to obtain the optimum non-axisymmetric end wall shape uses the idea of taking the information obtained from previous designs and using it in order to obtain a better behaved shape. In this optimization process, the chosen optimization algorithm is the genetic algorithm since it has the ability to enhance the capability of reaching the global minimum but with a drawback of needing thousands of iterations to do so. Artificial neural networks can be used to approximate the CFD computations since it would be to costly to perform a CFD computation for every geometry generated by the optimization algorithm. A database constituted by the design examples feeds the artificial neural network in what is known as the training of the ANN. As new design shapes are generated they are added to the database, updating it. After the update of the database, the ANN is subjected to a new learning step. This process follows until the predictions of the ANN are closer to what the actual CFD solution would be. The steps for the optimization process are the following (Figure 4):

- Creation of a meshing template for the grid generator using the meshing software Auto-Grid5 and IGG.
- Parameterization of the geometry to reduce the

geometrical degrees of freedom using the parameterization software Autoblade.

- Definition of the free and fixed geometrical parameters, generation of the initial database based on CFD simulations of arbitrary geometric samples using FINE/Design3D software.
- Definition of the optimization goals, run the optimization by means of the ANN, based on self-learning algorithm and performance check to compare the current sample with regard to the optimization goals using FINE/Design3D.

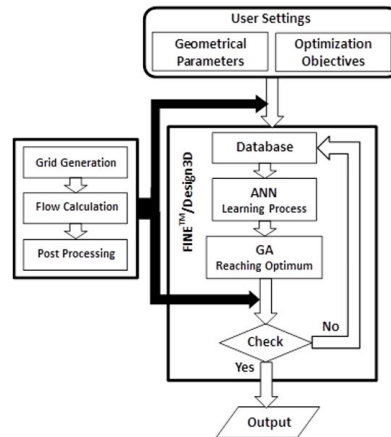


Figure 4: Flow Chart of the Optimization Process [8]

#### 3.1. End Wall Parameterization

In order to perform the non-axisymmetric end wall parameterization, the along channel parameterization method was used (Figure 5). This method creates cuts along virtual streamlines which are align with the blade camber curve. These cuts are divide equidistantly the blade passage. The parameterization area started upstream of the leading edge of the blade at the inlet interface while the end was set at the trailing edge of the blade. The blade channel was divided into 6 equidistant Bezier cuts. Each cut constituted by an equidistant distribution of 6 parameters. The choice of the number of parameters comes from the balance between predicted aerodynamic benefit and the computational cost of the optimization. Each parameter is limited to a movement normal to the end wall, i.e one-degree freedom. The allowed variation was of 6.75 mm which corresponds to 7.5% of the blade span. The value of the variation was chosen with respect to manufacturing constraints. Finally, the geometrical shape of the non-axisymmetric end wall is lofted through these cuts.

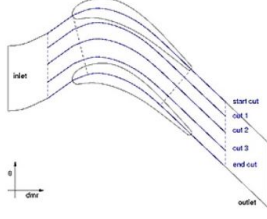


Figure 5: Along Channel Parameterization Method [10]

### 3.2. Grid Template

The grid generation procedure was performed using both AutoGrid and IGG meshing software from Numeca International. During the optimization procedure, both during the database generation and the ANN training/optimization several new geometries are generated and using the template and meshing scripts it is possible to automatically create the meshes for the new geometries. The template and meshing scripts are obtained through the mesh of the original geometry (reference geometry), i.e. geometry with axisymmetric end walls (Figure 6). It is required that the reference geometry and the modified geometries keep the same topology. In order to avoid poor quality meshes for the new geometries, the template mesh must have a grid quality as high as possible. Table 1 shows the number of mesh nodes for the stator and rotor.

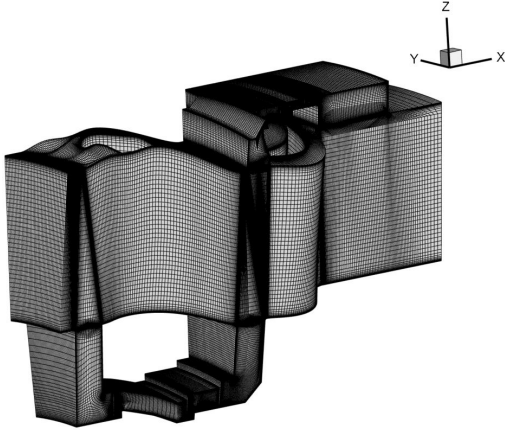


Figure 6: Mesh of the Original Geometry

	Stator	Rotor	Total
<b>Single-Pitch</b>	1.69	1.54	3.23

Table 1: Number of mesh nodes in millions rounded to two decimal digits

### 3.3. Optimization Objective

For the stator shroud end wall optimization, a study using three different objective functions was performed in order to see how the optimization results were going to differ through the use of different combination of strategies. Optimization's A objective function is defined by the combination of isentropic total-to-total efficiency and massflow. Optimization's B objective function is defined by the combination of isentropic total-to-total efficiency, massflow and entropy coefficient. Finally, Optimization C is performed using an objective function designed by the combination of isentropic total-to-total efficiency, entropy coefficient and secondary kinetic energy. The following equations represent the three objective functions used for the different optimizations.

$$OF_A = w_\eta P_\eta + w_{\dot{m}} P_{\dot{m}} \quad (1)$$

$$OF_B = w_\eta P_\eta + w_{\dot{m}} P_{\dot{m}} + w_{scoeff} P_{scoeff} \quad (2)$$

$$OF_C = w_\eta P_\eta + w_{\dot{m}} P_{\dot{m}} + w_{scoeff} P_{scoeff} + w_{SKE} P_{SKE} \quad (3)$$

Where,  $w$  are the weighting factors and  $P$  the penalty terms can be defined as:

- Equality constraint

$$P = \left( \frac{|Q_{imp} - Q|}{Q_{ref}} \right)^k \quad (4)$$

- Upper bound constraint if  $Q_{imp} > Q$  then

$$P = \left( \frac{Q_{imp} - Q}{Q_{ref}} \right)^k, \quad \text{else } P = 0 \quad (5)$$

- Lower bound constraint if  $Q_{imp} < Q$  then

$$P = \left( \frac{Q - Q_{imp}}{Q_{ref}} \right)^k, \quad \text{else } P = 0 \quad (6)$$

The optimum geometry will depend on how the objective function is chosen. Depending on the penalty terms and weighting factors, different optimum geometries will be obtained. In tables 2, 3 and 4 is summarized the chosen values for each different optimization.

	$\eta$ [%]	$\dot{m}_{max}$ [kg/s]	$\dot{m}_{min}$ [kg/s]
$Q_{imp}$	1	9.2034937	9.0212463
$Q_{ref}$	1	9.2034937	9.0212463
$\eta$		$\dot{m}_{max}$	$\dot{m}_{min}$
$w$	3	196	196
$k$	2	2	2

Table 2: Objective Function - Optimization A

	$\eta$ [%]	$s_{coff}$ [J/kg/K]
$Q_{imp}$	1	0
$Q_{ref}$	1	1
	$\dot{m}_{max}$ [kg/s]	$\dot{m}_{min}$ [kg/s]
$Q_{imp}$	9.2034937	9.0212463
$Q_{ref}$	9.2034937	9.0212463
	$\eta$	$s_{coff}$
$w$	1000000	2
$k$	2	2
	$\dot{m}_{max}$	$\dot{m}_{min}$
$w$	6833	6833
$k$	2	2

Table 3: Objective Function - Optimization B

	$\eta$ [%]	$s_{coff}$ [J/kg/K]
$Q_{imp}$	1	0
$Q_{ref}$	1	1
	$\dot{m}_{max}$ [kg/s]	$\dot{m}_{min}$ [kg/s]
$Q_{imp}$	9.2034937	9.0212463
$Q_{ref}$	9.2034937	9.0212463
	SKE [J/kg.K]	
$Q_{imp}$	0	
$Q_{ref}$	1	
	$\eta$	$s_{coff}$
$w$	1000000	2
$k$	2	2
	$\dot{m}_{max}$	$\dot{m}_{min}$
$w$	6833	6833
$k$	2	2
	SKE	
$w$	0.0024	
$k$	2	

Table 4: Objective Function - Optimization C

## 4. Results and Discussion

### 4.1. Stator Shroud Optimization - Optimization A

Table 5 shows how the objective function quantities for optimization A have changed when compared to the baseline geometry. The optimization procedure led to an efficiency increase of 0.99%. The massflow increased 1% compared to the baseline geometry case.

Variable	Baseline	Optimization A
$\eta_{tt}$	0.86112	0.86965
$\Delta\eta_{tt}$	-	+0.99%
$\dot{m}$	9.11237	9.20432
$\Delta\dot{m}$	-	+1%

Table 5: Variation of the Objective function quantities for Optimization A

Figure 7 is a representation of the end wall geometry for the best individual of optimization A. It shows the height variations as a percentage of the

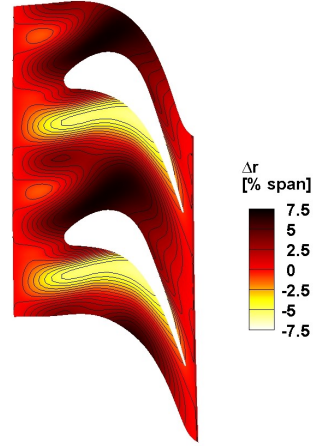
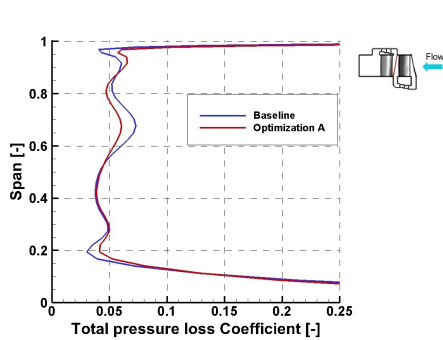


Figure 7: End wall radius variation, as percentage of span, for Optimization A

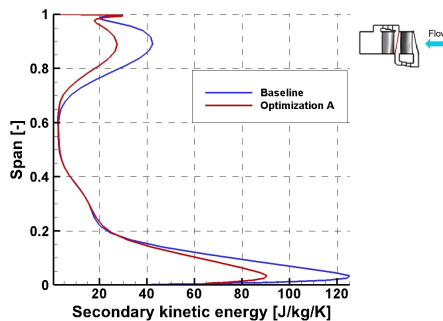
span. The optimized geometry is characterized by a concave region on the pressure side of the blade. The concavity starts early in the blade passage and propagates along the middle region. The suction side is characterized by a convex curvature in the early passage.

Figure 8 shows the pitchwise mass averaged total pressure loss coefficient and secondary kinetic energy at the stator exit. From Figure 8 a) we can see that although the end wall contouring was applied to the tip region, an increase of the losses in the region close to the tip end wall, from 90% to 99% of the span is verified. The optimized geometry shows a loss reduction in the mid/upper part of the span (approximately from 54% to 88% of the span). The radial distribution of the secondary kinetic energy (SKE) (Figure 8 b)) shows the reduction on the secondary flows intensity. The highest values for the SKE are found in the tip boundary layer and in the hub boundary layer. The peaks of SKE found at the tip and hub are associated with the secondary flow mechanisms. At the hub (at 4% of the span) we observe a peak in the SKE, which in the case of the contoured geometry has suffered a big reduction in the value of SKE (SKE reduction of 27.8%). Although the contour was applied to the tip, a reduction in the lower part of the span is also verified which comes to show that the end wall profiling not only affect the region close to the contour but also the flow along the entire span. The profiling was successful in the reduction of the secondary flows in the upper/midspan region (from 60% to 98% of the span). In this region of the span, the biggest reduction in loss was of 35.48%.

In order to give an explanation for the secondary flow loss reduction, the end wall static pressure coefficient ( $C_{pt}$ ) field is analyzed. Figure 9 shows a



(a) Pressure Loss Coefficient

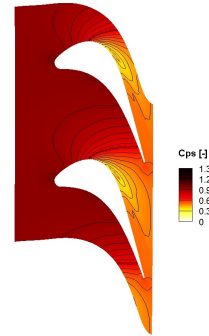


(b) Secondary Kinetic Energy

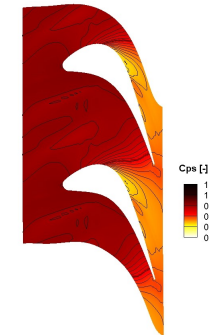
Figure 8: Pitchwise averaged Loss Distribution and Secondary Kinetic Energy at the stator exit for Optimization A

comparison between the end wall static pressure coefficient field for both the baseline and optimized geometry. When applying end wall contouring to a geometry, the pressure distribution suffers alterations generally resulting in a promoted crossflow in the early blade passage and a reduced cross passage pressure gradient in the late blade passage. These alterations on the pressure distribution potentially result in a reduction of the crossflow in the late passage resulting in a more uniform flow. When comparing both the baseline geometry (Figure 9 a)) and the optimized geometry (Figure 9 b)), one can see that the cross pressure gradient has suffered a reduction over the stator passage as a result of the end wall profiling. A reduction on the cross pressure gradient corresponds to a decrease in the passage vortex intensity.

It is known that the secondary flow structures have associated to them higher levels of entropy. Figure 10 shows the time-averaged entropy distribution at the stator exit and draws a comparison between the baseline and the optimized geometry. The areas where exists higher values of entropy, and therefore more intense secondary flow mechanisms, is in the hub and tip end wall zones. They correspond to the tip and hub leakage vortices. This cor-



(a) Baseline Geometry



(b) Optimized Geometry A

Figure 9: Tip End Wall Static Pressure Coefficient Contour - Optimization A

relates to the loss reduction observed previously in the midspan region, showing again that the tip profiling has the ability to change the flow field along the entire span and not only on the end wall region. In the tip region, where the end wall contouring was applied, the high values of entropy associated to the secondary flow mechanisms have been shifted to higher radial positions (Black Circle) when compared to the baseline geometry. The end wall profiling did not decrease the levels of entropy but shifted them closer to the tip end wall.

#### 4.2. Stator Shroud Optimization - Optimization B

In table 6 it is described how the analyzed quantities for this optimization have been altered when establishing a comparison with the baseline geometry. The end wall profiling of optimization B led to an isentropic total-to-total efficiency increase of 0.16%, which compared to the efficiency increase of 0.99% obtained in optimization A is far less impressive. Optimization B also led to a drop in the entropy coefficient of 0.051% and an increase of 0.018% in the massflow compared to the baseline geometry.

Figure 11 shows the end wall geometry for the best individual of optimization B. The optimized geometry is characterized by two concave regions on the pressure side of the blade. The suction side is characterized by a convex curvature in the early

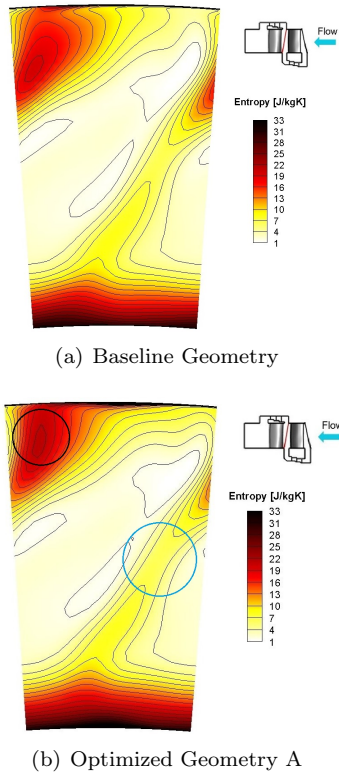


Figure 10: Time-averaged Entropy Distribution - Optimization A

Variable	Baseline	Optimization B
$\eta_{tt}$	0.86112	0.86247
$\Delta\eta_{tt}$	-	+0.16%
$\dot{m}$	9.11237	9.11403
$\Delta\dot{m}$	-	+0.018%
$s_{coeff}$	1.01180	1.01128
$\Delta s_{coeff}$	-	-0.051%

Table 6: Variation of the Objective function quantities for Optimization B

passage and by a small concavity in the middle region.

Similar to the analysis performed for optimization A, Figure 12 shows the pitchwise mass averaged total pressure loss coefficient and secondary kinetic energy at the stator exit. From Figure 12 a) we are able to assess that the losses have not be altered in the lower/midspan area, i.e the changes in the total pressure loss coefficient are only occurring from 51% of the span until the tip end wall at 100% of the span. In the case of optimization A there were still some alterations verified on the lower part of the span (around 20% of the span) as we can see in Figure 8. This is probably due to the fact that the resulting geometry of optimization B led to a end wall with lower values of the height change. The biggest loss reduction is occurring at 81% of the

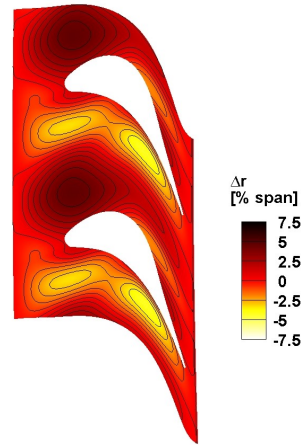
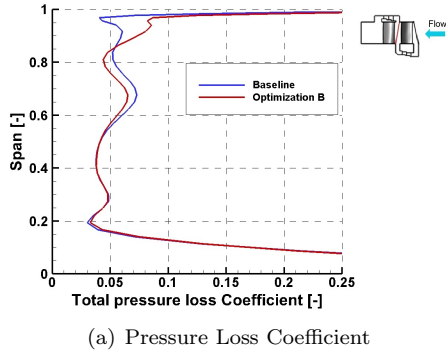


Figure 11: End wall radius variation, as percentage of span, for Optimization B

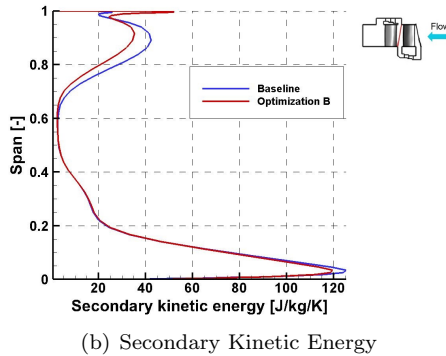
span with a reduction of 15.84% compared to the baseline. Figure 12 b) is a plot of the radial distribution of SKE where a comparison between the baseline and the optimized geometry can be established. The highest values of SKE occur in locations close to the tip and hub end wall, i.e in the tip and hub boundary layers. In the midspan region the values for the SKE are lower, which means that at this locations the flow is more homogeneous. The optimized geometry showed no differences to the baseline geometry in the region between 9% and 60% of the span. Although there is still a decrease in the values of the SKE for the profiled geometry in optimization B, they are not as significant as the reduction that optimization A provided. This shows that optimization B was less successful in the decrease of the intensity of the secondary flows, correlating to the fact that the efficiency increase was smaller when compared to optimization A.

The static pressure coefficient field (Figure 13) is characterized, in the suction side of the blade, by an increase in size of the area corresponding to the lower pressure when comparing to the baseline geometry. In the throat area region of the blade, the contoured geometry led to an alteration of the pressure isolines. The isolines had their orientation changed, becoming more perpendicular to the flow for the contoured case.

The time-averaged entropy distribution is plotted in Figure 14. Both in the baseline and the optimized geometry the hub and tip regions are the ones where the entropy values are the highest corresponding to areas of more significant secondary flow mechanisms. This correlates to the radial distribution of the SKE (figure 12 b)) where the tip and hub zones were the ones with the higher values of SKE. The optimized geometry shows an increase of the



(a) Pressure Loss Coefficient



(b) Secondary Kinetic Energy

Figure 12: Pitchwise averaged Loss Distribution and Secondary Kinetic Energy at the stator exit for Optimization B

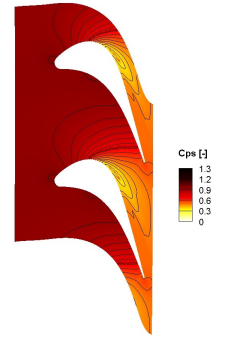
entropy close to the tip end wall when compared to the baseline geometry. It is also visible that the profiled geometry led to a shift of the higher entropy area to higher radial positions (white circle). In the upper/midspan region of the profiled geometry the entropy has suffered a small reduction (Blue circle).

#### 4.3. Stator Shroud Optimization - Optimization C

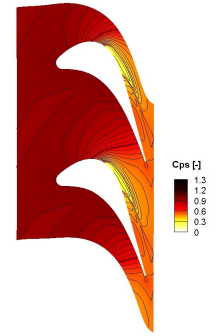
Table 8.3 shows how the analyzed quantities for this optimization have changed when compared to the baseline geometry. One can see that the optimization led to an efficiency increase of 0.94%, as well as to a drop in SSE of 23.86%. The massflow increased 0.86% and the entropy coefficient decreased 0.012% when comparing to the baseline geometry.

The end wall geometry for the best individual of optimization C is depicted in figure 15. It shows the height variations as a percentage of the span. The optimized geometry is characterized by a concave region on the pressure side of the blade and a convex region on the suction side of the blade, similarly to what was seen in optimization A (Figure 7). The first concavity occurs in the middle section of the passage. The suction side is characterized by a convex curvature in the early passage.

Although having different optimization objec-



(a) Baseline Geometry



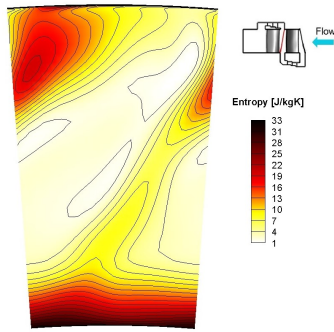
(b) Optimized Geometry A

Figure 13: Tip End Wall Static Pressure Coefficient Contour - Optimization B

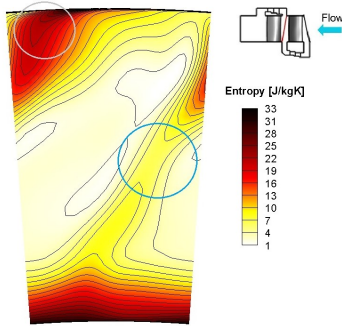
tives, optimization A and C produced similar end wall geometries. Not only were the geometries similar but their characteristics as well, e.g similar increase in efficiency and in the massflow. As a result, the behaviour showed by optimization C in the pitchwise mass averaged total pressure loss coefficient and secondary kinetic energy at the stator exit (Figure 16) correlates to the behaviour of optimization A.

Regarding the static pressure coefficient field (Figure 17), we can see that when comparing both the Baseline geometry (Figure 17 a)) and the Optimized geometry (Figure 17 b)) that the isolines in the suction side of the blade, especially in the early blade passage are closer to each other promoting the crossflow as expected. As it occurred in the end wall profiling of optimization geometry A, in the throat area region, the the pressure isolines are almost perpendicular to the profiled case. This alterations on the pressure distribution potentially result in a reduction of the crossflow in the late passage resulting in a more uniform flow.

Similarly to what occurred in optimization A, the time-averaged entropy distribution suffers a visible reduction in the midspan region (Blue circle). This correlates to the loss reduction observed previously in the midspan region. Close to the tip end wall, where the profiling was applied, the high values of



(a) Baseline Geometry



(b) Optimized Geometry B

Figure 14: Time-averaged Entropy Distribution - Optimization B

entropy associated to the secondary flow mechanisms have been shifted to higher radial positions (Black Circle).

## 5. Conclusions

With optimization A, the total-to-total efficiency was increased by 0.99%. This increase is a result of the improvement of the flow. At this region, the delta in total pressure loss coefficient has suffered a significant reduction of 21.1% when compared to the baseline geometry. The secondary kinetic energy was significantly reduced both in the hub and tip region. At the hub, a reduction of 27.8% occurs, as for the tip the end wall contouring was successful in the reduction of the secondary flows in the span region from 60% until 98%. In this region of the span, the biggest reduction in loss was of 35.48%. The end wall contouring also led to changes in the pressure gradient at the tip end wall. The cross pressure gradient, which is the driver of the passage vortex, suffered a reduction culminating in a more uniform flow and in a suppression of a separation structure present in the pressure side of the blade. The end wall contouring also decreased the pressure gradient from tip to hub. This reduction leads to less mixing losses and a more uniform flow along the span. This phenomena is a reason to why there was a reduction of the losses in the midspan

Variable	Baseline	Optimization C
$\eta_{tt}$	0.86112	0.86924
$\Delta\eta_{tt}$	-	+0.94%
$\dot{m}$	9.11237	9.19065
$\Delta\dot{m}$	-	+0.86%
$s_{coeff}$	1.01180	1.01168
$\Delta s_{coeff}$	-	-0.012%
$SKE$	26.83134	20.42972
$\Delta SKE$	-	-23.86%

Table 7: Variation of the Objective function quantities for Optimization C

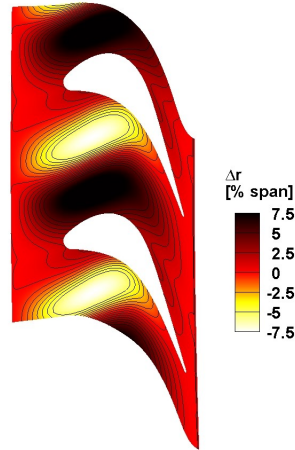
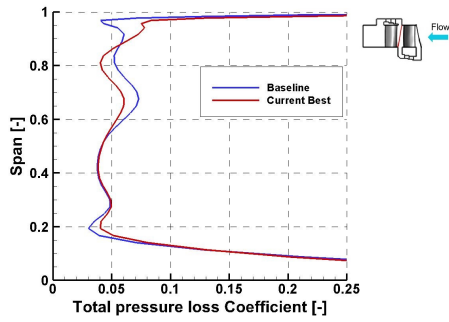


Figure 15: End wall radius variation, as percentage of span, for Optimization C

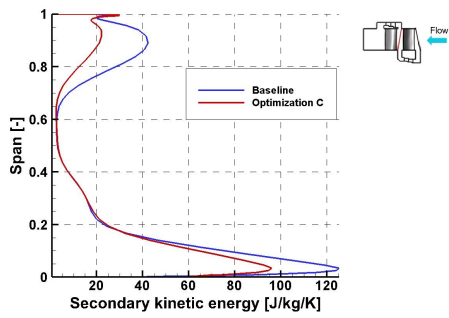
region.

Optimization B allowed the total-to-total efficiency to increase by 0.16%. An increase far less impressive than the one verified for optimization A. The biggest reduction in the loss coefficient was of 15.84% and happened at 81% of the span. Compared to the 35.48% reduction in optimization A, the decrease here is quite smaller. However, optimization B was successful in the decrease of the underturning and overturning from 50% of the span until 100%, where the values of the profiled geometry were always lower than the values of the baseline geometry. Below 50% of the span, the contoured geometry had the same behaviour as the baseline geometry.

Finally, optimization C resulted in a total-to-total efficiency increase of 0.94%. This optimization has shown to be really similar to optimization A, not only in the value of the efficiency increase but in the behaviour of the flow. Both optimizations A and C produced similar end wall geometries, both are characterized by the existence of a concave region on the pressure side and a hill on the suction side of the blade. The efficiency increase comes as a result of the improvement of the flow. At 81%



(a) Pressure Loss Coefficient



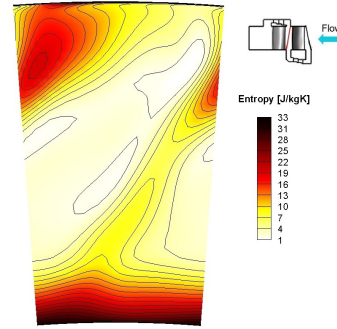
(b) Secondary Kinetic Energy

Figure 16: Pitchwise averaged Loss Distribution and Secondary Kinetic Energy at the stator exit for Optimization C

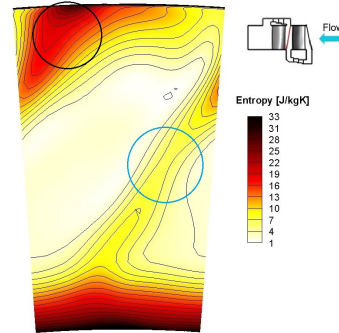
of the span, the total pressure loss coefficient has decreased 22.72% in comparison to the baseline geometry. The SKE also showed similar behaviour to what was verified in optimization A. The increase in efficiency comes from the reduction of both the cross pressure gradient at the tip end wall and the reduction of the tip to hub pressure gradient. These pressure gradients are the drivers of the secondary flows and a reduction in the gradient results in a more uniform flow along the span.

## References

- [1] P. Schupbach. *Influence of Rim Seal Purge Flow on the Performance of an Endwall-Profiled Axial Turbine*. Doctoral thesis, Swiss Federal Institute of Technology (ETHZ), 2009.
- [2] W R Hawthorne. Secondary Circulation in Fluid Flow. *Proceedings of the Royal Society of London. Series A, Mathematical and Physical Sciences*, 206(1086):374–387, 1951.
- [3] L. S. Langston, M. L. Nice, and R. M. Hooper. Three-Dimensional Flow Within a Turbine Cascade Passage. *ASME Journal Engineering for Power*, 99(1):21–28, 1977.



(a) Baseline Geometry



(b) Optimized Geometry C

Figure 17: Time-averaged Entropy Distribution - Optimization C

- [4] Phil Ligrani, Geoffrey Potts, and Arshia Fatemi. Endwall aerodynamic losses from turbine components within gas turbine engines. *Propulsion and Power Research*, 6(1):1–14, 2017.
- [5] Thomas Ernst Biesinger. *Secondary flow reduction techniques in linear turbine cascades*. Doctoral thesis, Durham University, 1993.
- [6] S Harrison. The Influence of Blade Lean on Turbine Losses. *ASME Journal of Turbomachinery*, 114(1):184–190, 1992.
- [7] G. Rioulet. Curved channels through which a gas or vapour flows, September 22 1970. US Patent 3,529,631.
- [8] Zhenzhe Na and Bo Liu. Numerical Investigation of Non-Axisymmetric Endwalls in a High Pressure Axial Flow Turbine. *ASME Turbo Expo: Power for Land, Sea, and Air*, 2A:1–11, 2015.
- [9] Steffen Reising. *Steady and Unsteady Performance of a Transonic Compressor Stage with Non-Axisymmetric End Walls*. PhD thesis, Technical University of Darmstadt, 2010.
- [10] International Numeca. User Manual FINE/Design3D v.11.2, 2017.